

## MICROSTRUCTURAL EVOLUTION AND MECHANICAL PROPERTY–FRACTAL BEHAVIOR RELATIONS OF AN AGED SUPER DUPLEX STAINLESS STEEL

O.A. Hilders<sup>a,b,\*</sup>, N. Zambrano<sup>c</sup> †, J. L. Ochoa M.<sup>d</sup>

<sup>a</sup>Departamento de Metalurgia Física, Escuela de Ingeniería Metalúrgica y Ciencias de los Materiales, Universidad Central de Venezuela (UCV), Apartado 47514, Caracas 1041-A, Venezuela.

<sup>b</sup>Profesor—Investigador Visitante, Laboratorio de Medidas Eléctricas en Materiales, Centro de Ingeniería de Materiales y Nanotecnología, Instituto Venezolano de Investigaciones Científicas (IVIC), Apartado 21827, Caracas, 1020-A, Venezuela.

<sup>c</sup>Fundación para el Desarrollo Profesional del Colegio de Ingenieros de Venezuela, Caracas 1050, Venezuela. † (Fallecido).

<sup>d</sup>Laboratorio de Medidas Eléctricas en Materiales, Centro de Ingeniería de Materiales y Nanotecnología, Instituto Venezolano de Investigaciones Científicas (IVIC), Apartado 21827, Caracas, 1020-A, Venezuela.

\*Corresponding Author, e-mail: ohilders@hotmail.com, Tel-Fax: +58 212 3725230.

Received: November 2016. Accepted: October 2017.

Published: July 2018.

### ABSTRACT

We studied the relation between the mechanical properties and the fractal dimensional increment for 40 V–notch Charpy and 16 round tensile samples of SAF 2507 super duplex stainless steel, aged between 0 and 288 h at 475 °C, and broken at room temperature. A variety of techniques such as optical microscopy, scanning electron microscopy and image analysis were used to study the microstructure and the nature of the fracture surfaces, whereas the values of the fractal dimensional increment [ $(D_T)^*$  for tension and  $(D_I)^*$  for impact], were determined using the slit island method. The relation between impact toughness  $I$ , and  $(D_I)^*$  was of a linear positive type and the impact fracture surfaces showed a transition from ductile to brittle behavior for increased aging times. As the impact fracture surfaces become brittle, numerous cleavage cracks nucleate in the embrittled ferrite, but their propagation is controlled by the austenite, which remains ductile. Tension tests reveal that the strength of the material increases as the time of aging increases while ductility slightly decreases. Tension fracture surfaces were of the ductile type, and it was impossible to distinguish one from the other on a qualitative basis. Then, specification of  $(D_T)^*$  can be successfully used to discriminate between very similar fracture surface morphologies which correspond to different values of strength and ductility, both, in SAF 2507 as well as in many other metallic alloys.

**Keywords:** Fractal dimensional increment, impact toughness,  $\alpha'$  phase, 475 °C embrittlement.

### EVOLUCIÓN MICROESTRUCTURAL Y RELACIÓN ENTRE LAS PROPIEDADES MECÁNICAS Y EL COMPORTAMIENTO FRACTAL EN UN ACERO INOXIDABLE SUPER DUPLEX ENVEJECIDO

#### RESUMEN

Hemos estudiado la relación entre las propiedades mecánicas y el incremento dimensional fractal para 40 probetas entalladas Charpy y 16 probetas cilíndricas de tracción, del acero inoxidable super duplex SAF 2507 envejecido entre 0 y 288 h a 475 °C y fracturado a temperatura ambiente. La microestructura y la naturaleza de las superficies de fractura fueron analizadas mediante microscopía óptica, microscopía electrónica de barrido y análisis de imágenes, mientras que los valores del incremento dimensional fractal [ $(D_T)^*$  para tensión y  $(D_I)^*$  para impacto], se determinaron mediante el método de las islas. La relación entre la tenacidad de impacto  $I$ , y  $(D_I)^*$  fue de tipo lineal positivo, y las superficies de fractura por impacto mostraron una transición dúctil–frágil con el aumento del tiempo de envejecimiento. En la medida en que las superficies de fractura por impacto se hacen más frágiles, numerosas grietas de clivaje se nuclean en la ferrita, aunque su propagación es controlada por la austenita, que permanece dúctil. La resistencia en tensión de este material aumenta con el aumento del tiempo de envejecimiento, mientras que la ductilidad apenas disminuye. Todas las superficies de fractura por tensión fueron de tipo dúctil, resultando imposible distinguir las entre sí. Luego, la especificación de  $(D_T)^*$  puede ser útil para distinguir morfologías de fractura muy similares que correspondan a diferentes valores de resistencia y ductilidad, tanto en el acero objeto de estudio, SAF 2507, como en otras aleaciones metálicas.

**Palabras claves:** Incremento dimensional fractal, tenacidad de impacto, fase  $\alpha'$ , fragilidad de 475 °C.

## INTRODUCTION

Super duplex stainless steels (SDSS) are a class of steels with a mixed crystal structure composed by approximately equal amounts of austenite  $\gamma$ , and ferrite  $\alpha$ . These steels combine an excellent corrosion resistance in most of the in-service conditions with a good mechanical properties [1-4]. Particularly, SDSS grades have enhanced pitting and crevice corrosion resistance when compared with the common austenitic or ferritic stainless steels grades [5,6]. This can be attributed to the improved levels of several elements like chromium, molybdenum and nitrogen found in these alloys [7], making them the best choice for many applications as structural materials in critical components of nuclear power plants [8-10], chemical [11,12], petroleum and gas industries [13-14], transportation [15], desalination plants [16,17], etc. However, these steels are unsuitable for several engineering applications when exposed in the temperature range of 280–500 °C, which produces enhanced hardness but reduces ductility and toughness [18-19]. This phenomenon is termed “475 °C embrittlement” as the rate of embrittlement is highest at this temperature [20-23]. The fatigue [24-27], tensile [28-31], and fracture [32-34] properties of these steels are affected by the process of embrittlement.

Corrosion resistance is also affected with aging at 475 °C. The degradation in corrosion resistance and mechanical properties of these alloys during the aging is attributed to the spinodal decomposition of the ferritic phase to chromium-rich phase ( $\alpha'$ ) and iron-rich phase ( $\alpha$ ) in the mentioned temperature range, due to the presence of a miscibility gap in the iron-chromium binary alloy system. The precipitation of the chromium-rich phase  $\alpha'$ , results in a Cr depletion in the surroundings of this phase which embrittles the microstructure ( $\alpha$  phase), generating a localized corrosion attack after aging treatments [35,36]. Because the precipitation of the phase  $\alpha'$  at 475 °C only occurs in the ferrite phase, early investigations were confined only to the binary iron-chromium alloys, and to several commercial grades of ferritic type stainless steels

[37,38]. The microstructure of SDSS allows them to obtain high strength and toughness levels [39-41] and good resistance to localized corrosion and stress corrosion cracking [42,43]. In addition to the higher mechanical strength and superior resistance to corrosion, when SDSS are compared with austenitic steels, another advantage is apparent, namely, a lower price, as SDSS have lower nickel content [44]. On the other hand, since nitrogen stabilized the austenite, as nickel does, there has been an increased use of nitrogen to replace nickel in SDSS. In general, the major interest in SDSS is related with their high resistance to chloride induced corrosion, which is a problem in many marine and petrochemical applications [45], and with the great improvements that can be achieved in weldability, by reducing the carbon content and simultaneously increasing the nitrogen content [46].

The present paper will be concerned with the correlation between some mechanical properties in tension, impact toughness, and fractal characteristics of the SDSS SAF 2507, after aging treatments at 475 °C, in order to provide some quantitative estimates related with the degree of embrittlement, which can be useful for future correlations with corrosion behavior. In other words, as resistance to corrosion is affected by the embrittlement of the ferrite phase in SDSS, the data concerned with the evolution of embrittlement (change in mechanical properties, degree of tortuosity of the fractured surfaces as measured by the fractal dimensional increment, etc.) can be used to explain the corrosion behavior of the studied alloy.

## MATERIALS AND METHODS

### Material and Heat Treatments

The material used in this work was a commercially produced super duplex stainless steel, designated SAF 2507 (UNS S32750, F53), and fabricated by Sandvik Materials Technology. The composition of the studied alloy (wt pct) is: 22Cr; 4.5Ni; 2.5Mo; 2.0Mn; 1.0Si;

0.03P; 0.02S; 0.10 N; 0.03C; and Fe (balance). Figure 1 shows the duplex microstructure composed of island-shaped austenite phase, and the band-shaped ferrite matrix ( $\gamma$  and  $\alpha$  respectively). Behara's reagent (20 ml HCl, 40 ml H<sub>2</sub>O and 0.5 g K<sub>2</sub>S<sub>2</sub>O<sub>5</sub>) was used to reveal the microstructure, which in turn was digitally enhanced. Several cylindrical hot-rolled bars of 25.4 mm diameter of the studied alloy were used to pre-prepare 40 standard Charpy V-notch impact samples, and 16 round tensile specimens of 25.4 mm gage length. Both, Charpy and tensile samples were solution treated at 1100 °C for 30 min, and quenched in water to room temperature. Subsequently, 35 Charpy samples out of 40 and 14 tensile samples out of 16, were isothermally aged at 475 °C for 3, 9, 24, 72, 120, 192 and 288 h (5 Charpy and 2 tensile samples for each time of aging respectively), quenching in water, and then left to cool in air to room temperature. The 7 remaining unaged samples (5 Charpy and 2 tensile samples), represent the "0 h aging" for each case.

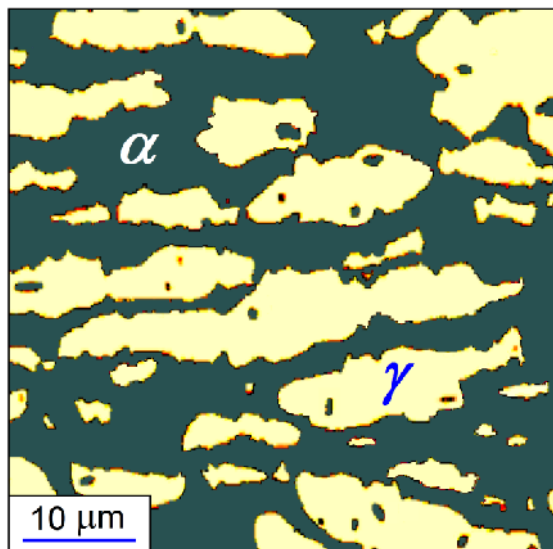


**Fig. 1.** Optical micrograph of the as-received microstructure of SAF 2507 SDSS.

### Uniaxial Tensile Tests and Charpy Impact Tests

After aging treatments, all impact and tensile specimens were tested at 25 °C, in a universal impact test machine and using an Instron screw-driven testing machine

respectively. Five replicate impact tests were done for each time of aging [47], and uniaxial tensile tests were conducted at 25 °C in displacement control, at a nominal strain rate of  $1.7 \times 10^{-4} \text{ s}^{-1}$  [48]. For tensile samples, two replicate tests were done for each time of aging. A computerized data logger was used in order to monitor and store the axial strain and the applied load.

### Microstructural Analysis

Eight metallographic samples were machined from the original cylindrical hot-rolled bars and solution treated for 1 h at 1100 °C. Then, 7 samples out of 8 were aged, one at the time, at 475 °C for the same duration than the impact and tensile samples. On completion of the heat treatments, all the samples, including the remaining "0 h aging sample" (wrought condition: as-received + solution treated) were mounted, ground and polished using standard metallographic methods. The corresponding microstructures were revealed by mechanical etching, using Behara's reagent. Both, transverse and longitudinal sections of the metallographic samples were studied to determine the evolution of the microstructure (Figure 2).

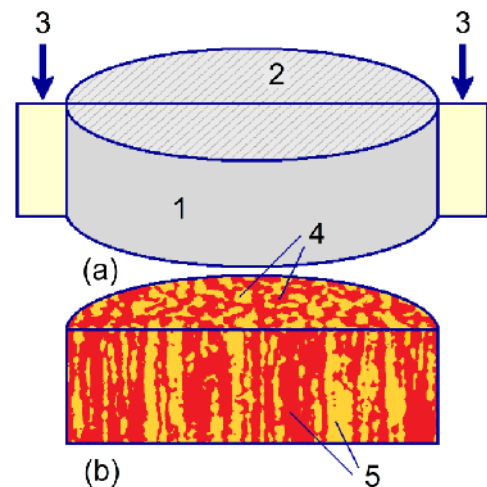


**Fig. 2.** Schematic of a metallographic sample and the two mutually perpendicular sections of analysis. (a) 1: external surface of the uncut sample, 2: uncutting surface of the cross section, 3: cutting plane. (b) 4 and 5: duplex microstructure. Ferrite: red, austenite: orange.

Several differences in morphology between ferrite and austenite were highlighted in figure 2, showing the ferrite matrix colored in red and the austenite islands in orange. Microstructural analysis of the samples was conducted in a light optical microscope, equipped with a 35 mm film camera, and also with an automatic image analyzer.

### Fractography

Observations and analysis of the fracture surfaces of broken tensile and impact samples were carried out using a scanning electron microscope (SEM) operated at 20 Kv. The cup portions of the fractured tensile samples were removed and analyzed in the central region. On the other hand, the section of the impact samples where fractographs were taken and analyzed was the middle zone, specifically the very center of this location, avoiding shear lips zones, borderlines or the edges of the samples.

### Fractal Geometry

The fractal geometry approach has proven to be very useful to study the relation between fracture surface characteristics and mechanical properties [49–58]. Fractal analysis was carried out on the fracture surfaces of both, the standard Charpy V–notch, and the round tensile specimens. The fractal dimensional increment  $D^*$ , or fractional part of the fractal dimension  $D$ , was used in the characterization of the fracture surfaces. For impact and tension fracture surfaces  $D^* = (D_i)^*$  and  $D^* = (D_T)^*$  respectively.

The values of the fractal dimensional increment were determined according to the so called “slit island method” (SIM) [49,51,55,57,59]. The broken impact and tension samples, one for each experimental condition, were cold molding using epoxy. For each case the epoxy was pouring over the sample, which was previously attached to a cylindrical support. Each sample was positioned faceup, allowing the epoxy to cover the entire fracture surface. Grinding and polishing operations parallel to the mean plane of fracture were done, developing a number of

successive layers in which parts of the fracture surface become visible (“islands”). As the layers increase in number, the islands do, and growth and coalescence of islands take place. For a particular  $j$ th layer with  $n$  islands,  $P_i$  and  $A_i$  represent the perimeter and the area of the  $i$ th island respectively, so taking into account all the islands in this layer, the total perimeter and the total area are  $\sum P_i$  and  $\sum A_i$ . For all the layers, a full logarithmic scale diagram of  $\sum P_i$  vs  $\sum A_i$  leads to a straight curve, from which the fractal dimension  $D$  can be deduced. As the general fractal dimensional increment is:  $D^* = D - 1$  and  $D = 2 \times \text{slope}$  [being the slope:  $m = d(\log \sum P_i) / d(\log \sum A_i)$ ], then, the fractal dimensional increment representing  $(D_i)^*$  or  $(D_T)^*$  is:

$$D^* = 2 \left\{ d \left[ \log \sum_{i=1}^n (P_i) \right] / d \left[ \log \sum_{i=1}^n (A_i) \right] \right\} - 1$$

(1)

Image processing was performed by optical microscopy, and image analysis. Following Carney *et al.*, [55], if the used image analysis program is unable to accurately distinguish the boundary of a particular island from its surroundings, then the island was printed for contrast enhancement, re-scanned and digitally analyzed. Examples showing islands before digitalization can be seen in figure 3.

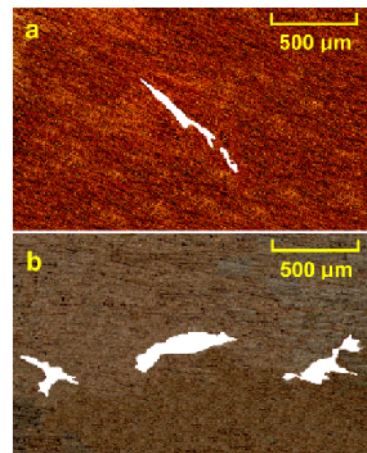


**Fig. 3.** Metallic islands before final digitalization. (a) Island of a broken impact sample aged for 24 h. (b) Group of islands of a broken unaged impact sample.

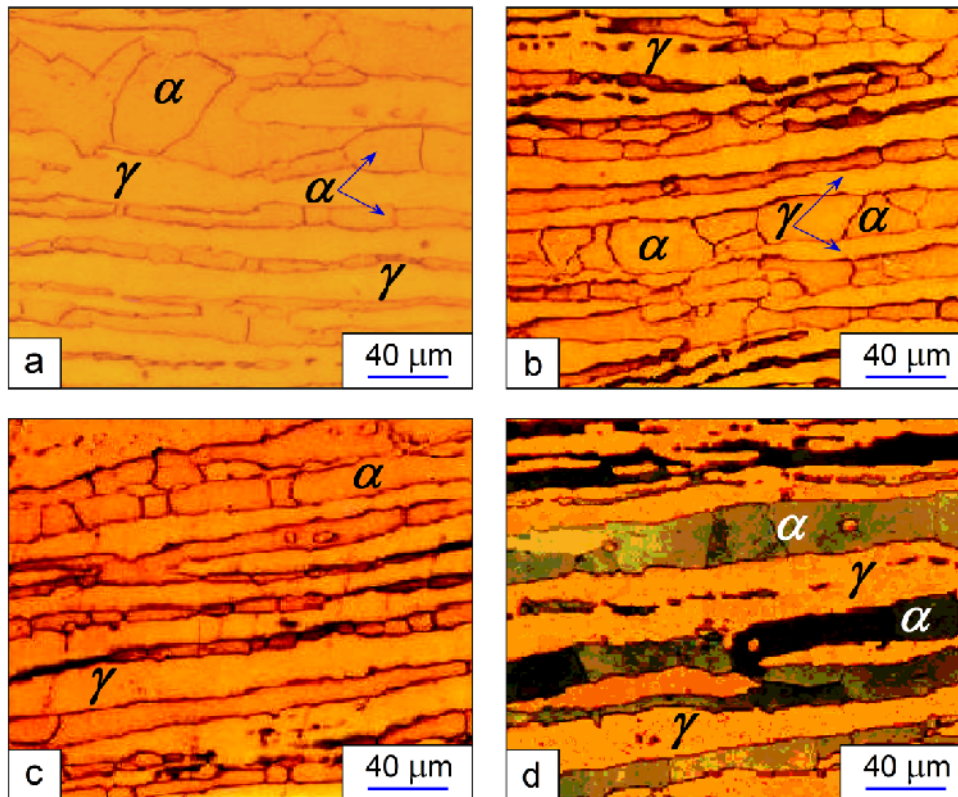


**Fig. 4.** Optical micrographs of the microstructures corresponding to the SAF 2507 SDSS. (a) “0 h of aging” (as–received + solution treated), (b) Aged for 3 h, (c) Aged for 9 h, (d) Aged for 24 h.

## RESULTS AND DISCUSSION

### Analysis of the Microstructures

The microstructural evolution of the studied steel for the low times of aging is presented in figure 4 (“0 h aging”, 3, 9, and 24 h). Figure 4–a (“0 h aging”), shows the grain boundaries of the ferrite and the interfaces  $\gamma/\alpha$  outlined after chemical attack. As the BCC crystalline structure of the ferrite is much emptier than the FCC crystalline structure of the austenite, the  $\gamma$  grain boundary attack has been prevented. The microstructures in figures 4–b and 4–c (3 and 9 h of aging respectively) are almost identical, and show a better definition of the grain boundaries of ferrite and the interfaces  $\gamma/\alpha$ , than that of the “0 h aging” condition, for the same time of attack. It suggests that precipitation of phase  $\alpha'$  occurs at 475 °C, before the minimum time of 9 h for its formation, reported by Nilsson [46], which is based on the construction of the SAF 2507 TTT phase diagram made by Wilson below 700

°C [60]. Several analyses of the microstructures reported in figure 4 show a volume fraction of 47% ferrite and 53% austenite. This finding reveals that the possible formation of  $\alpha'$  phase for these low times of aging, does not influence the approximate 50/50 ferrite to austenite volume fraction of the as–received duplex microstructure. Figure 4–d shows a typical view of the microstructure after 24 h of aging. It is apparent the thickening of both, the ferrite and the austenite phase, which can be ascribed to the process of coarsening due to the relative high holding time of 24 h at 475 °C. For this condition, the darkening of the ferrite, which is also apparent, denotes an increased degree of precipitation of the phase  $\alpha'$ , since as this phase increases in volume for longer times of aging, local changes in composition occurs because of the partitioning of Cr and

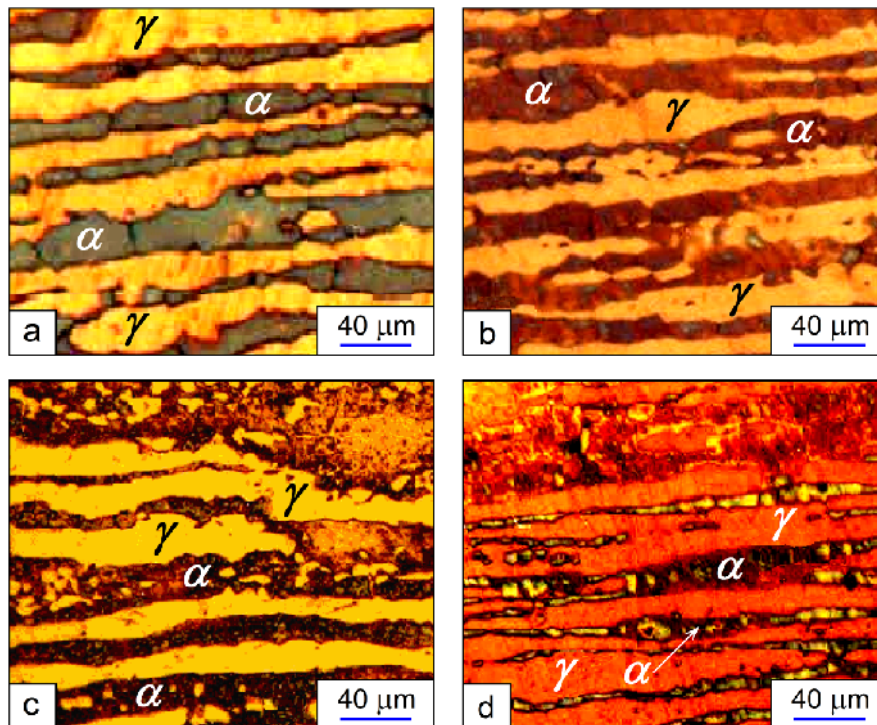


**Fig. 5.** Optical micrographs of the microstructures corresponding to the SAF 2507 SDSS. (a) Aged for 72 h, (b) Aged for 120 h, (c) Aged for 192 h, (d) Aged for 288 h.

Fe to the ferrite phase. This partitioning takes place when phase  $\alpha'$  precipitates according to  $\alpha \rightarrow \alpha + \alpha'$  [61,62]. Note that the formation of the chromium-rich phase  $\alpha'$  only takes place in the ferrite, mainly because the diffusivity of Cr in the BCC crystalline structure of the  $\alpha$  phase, is much higher than in the FCC crystalline structure of the  $\gamma$  phase [16,63]. It is believed that the  $\alpha'$  precipitation takes place by spinodal decomposition or nucleation and growth [16, 64, 65]. Irrespective of the reaction by which  $\alpha'$  is formed it results in an embrittlement of the ferrite phase, an increase in hardness, and a degradation of the general resistance to corrosion.

Some characteristics of the  $\alpha'$  precipitate were studied as early as 1953 by Fisher *et al.*, [66], who determined that this phase was a nonmagnetic BCC structure, with a spherical morphology, a diameter of  $\approx 200 \text{ \AA}$ , a composition of  $\approx 80 \text{ at\% Cr}$  and a lattice parameter between that of iron ( $a_{\text{Fe}} = 2.867 \text{ \AA}$ ) and chromium ( $a_{\text{Cr}} = 2.884 \text{ \AA}$ ). Taking into account the very low elastic coherent strain energy of the  $\alpha/\alpha'$  interface [due to the

0.59% difference in the atomic size of iron and chromium:  $((a_{\text{Cr}} - a_{\text{Fe}}) / a_{\text{Fe}}) \times 100 = ((2.884 - 2.867) / 2.867) \times 100 = 0.59\%$ ] it is clear that this two-phase mixture must be interconnected without directionality (isotropic spinodal structure), making the identification of the interface very difficult. Using atom probe field ion microscope (APFIM), the probable existence of a 3D interconnected network structure of the  $\alpha'$  phase has been suggested by Miller and Bentley [67]. As the time of aging at  $475 \text{ }^\circ\text{C}$  increases, the  $\alpha'$  network is extended all over the ferrite, allowing an increase in brittleness of this phase.

The evolution of the duplex microstructure of the SAF 2507 SDSS between 72 and 288 h is shown in figure 5. The 72 and 120 h of aging conditions (Figures 5–a and 5–b respectively) reveal very similar microstructure morphology of the ferrite and austenite phases, which still show highly elongated phase domains, aligned parallel to the axis of rolling. As can be seen,  $\gamma$  phase remains with no signs of etching since precipitation of  $\alpha'$  phase takes

place only in  $\alpha$ , making this phase a more energetic site to the chemical attack of Behara's reagent. For extending aging times some austenitic islands into the ferritic domains become finer and disconnected, *i.e.* the austenite becomes fragmented as can be seen in figure 5–c (192 h of aging). On the other hand, the ferrite areas become deeply etched, showing a very dark coloration. For the longest aging time of 288 h (Figure 5–d), a complete change in the ferrite morphology, which consists in the thinning, bulging and fragmentation of the ferrite bands, was observed. All these effects can be related with the formation of the alternate regions, rich and poor in chromium ( $\alpha'$  phase), inside the ferrite phase.

### Tensile Fracture Behavior

Nilsson *et al.*, [68], reported that the ductility of the duplex stainless steels family is quite good even in the presence of the  $\alpha'$  phase. This finding is very important, especially for applications that involve static loads. In the pre-sent work, the tensile ductility (% Elongation), barely decreases from 32.8% ("0 h aging") to 26.3% (288 h of aging). According to Verhaeghe *et al.*, [69], the  $\alpha$  phase controls the strength in SDSS and duplex stainless steels (DSS). Tensile deformation in  $\alpha$  is quite homogeneous for the solution treated condition, but for higher times of aging, when the strength increases, the deformation becomes more localized and the ductility slightly decreases. Mcirdi *et al.*, [70], have shown that the local stress on the ferrite grains  $\sigma_f$  (second order stress on mesoscopic scale), is higher than that of the  $\gamma$  grains  $\sigma_a$  and then the applied macroscopic stress  $\sigma$  ( $\sigma$  is a first order stress which concerns to the polycrystalline material as a whole). This is explained by the formation of  $\alpha'$  phase in the ferrite.

The results recorder in Table 1 confirm the described tendencies for the strength (Proof strength,  $R_{p0.2\%}$ , and Tensile strength,  $R_m$ ), and ductility [% Elongation,  $El(\%)$ ] obtained in the present work.

**Table 1.** Mechanical properties in tension

t (h)	0	3	9	24	72	120	192	288
$R_{p(0.2\%)} (MPa)$	614	661	692	721	740	778	805	854
$R_m (MPa)$	723	777	805	820	890	922	935	972
$El(\%)$	32.8	32.7	32.4	32.1	31.0	29.1	27.1	26.3

Hilders *et al.*, [28], obtained similar results for a 2205 DSS aged between 1 and 120 h at 475 °C. Verhaeghe *et al.*, [69], observed that austenite phase deforms first, and the slip is easily translated to the ferrite only for a coherent type of the interface  $\gamma/\alpha$ . In this case, the crystallographic relation between ferrite and austenite is that of the Kurdjumov–Sachs:  $\{110\}_\alpha // \{111\}_\gamma$  and  $\langle 111 \rangle_\alpha // \langle 110 \rangle_\gamma$ . For a random orientation between  $\alpha$  and  $\gamma$ , Zie-linsky *et al.*, [71], have shown that the incompatibility between the slip systems of both phases results in the cross slip of the dislocations emitted from the  $\gamma/\alpha$  boundary into the ferrite, inducing the formation and multiplication of dislocation loops, which in turn generate an increase of strength and a decrease in ductility. This effect is increased for the amount of  $\alpha'$  which is larger for higher times of aging, leading to an increased resistance to the dislocation motion into the ferrite. As the compatibility of easy slip systems in the two phases is much less common than the corresponding random orientation between  $\alpha$  and  $\gamma$  through the interface, the second mechanism has more chance to occurs. The effect of aging treatment between 0 and 288 h at 475 °C on tensile properties of SAF 2507 SDSS is shown in figure 6. On the other hand, figure 7 shows the macroscopic tensile fracture surfaces associated with just four representative times of aging (3, 24, 192 and 288 h), as the same ductile morphology was present in all the experimental conditions. The macroscopic fracture was of the cup–and–cone type, developed for axisymmetric conditions [72].

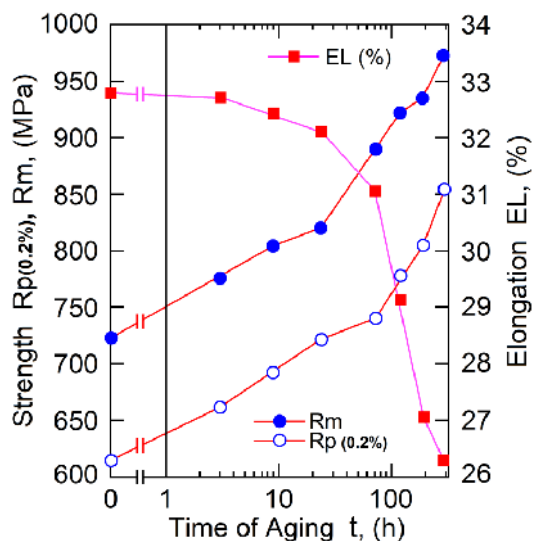


**Fig. 6.** Strength and ductility of the SAF 2507 SDSS as a function of the aging time at 475 °C.

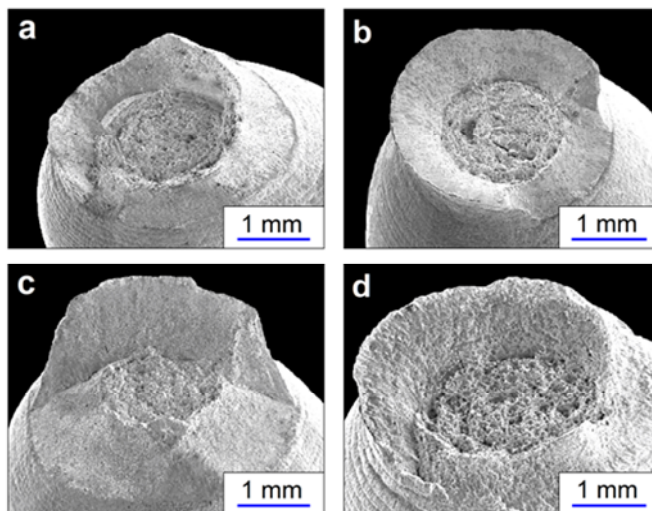


**Fig. 7.** Examples of the macroscopic tensile fracture surfaces (SEM) of the SAF 2507 SDSS aged for: (a) 3 h, (b) 24 h, (c) 192 h, (d) 288 h.

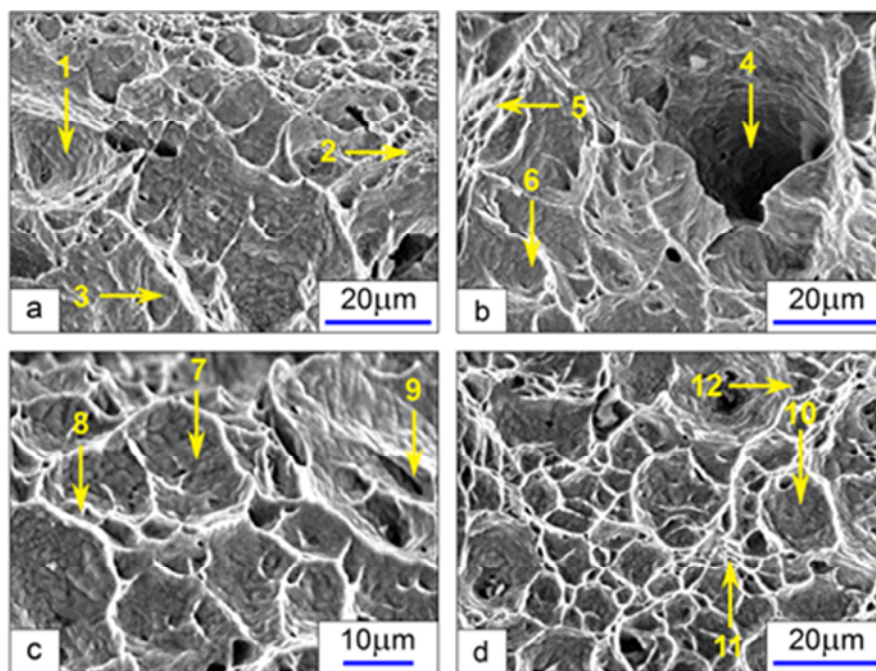


**Fig. 8.** Microscopic SEM fractographs of the broken tensile samples of SAF 2507. (a) Aged for 3 h, (b) Aged for 24 h, (c) Aged for 192 h, (d) Aged for 288 h. The numerical sequence in each figure [for example: (1,2,3), (4,5,6), etc., represents: An equiaxed dimple; a void sheet and a parabola-shaped dimple respectively.

Figure 8 shows the microscopic nature of the fracture surfaces, corresponding to the experimental conditions of figure 7 (the fracture surfaces for the eight times of

aging, presented the very same mechanism of rupture). In general, these fracture surfaces are of the ductile type. A large number of dimples have been developed, covering

all the area of the fractured surfaces. As it is very well known, this mechanism of fracture is called “nucleation, growth and coalescence of microvoids” or “microvoid coalesce” (MC) for short [73,74]. Three typical features of tension ductile fracture by MC are present in the fractured surfaces showed in figure 8 namely, (a) the regular equiaxed dimples characteristic of a rupture by “normal

separation” (Mode I); (b) groups of small voids (void sheets) formed between large voids generated at an earlier stage of the deformation process and (c) some parabola-shaped dimples formed by locally developed “shear rupture” (Mode II). All these three features have been showed by arrows in figure 8, in a numerical sequence for each one of the represented conditions.

**Table 2.** Impact energy data for different times of aging at 475 °C

Time t, (h)	0	3	9	24	72	120	192	288
Impact Toughness $I$ , (J)	300.00	300.00	296.31	296.18	198.31	146.19	109.81	69.14
	300.00	300.00	295.91	287.98	197.55	136.21	107.27	64.61
	300.00	298.50	282.69	272.21	214.93	124.00	101.42	41.70
	299.50	297.10	278.43	239.41	190.15	115.90	81.00	21.12
	299.10	295.81	269.91	173.17	169.66	112.00	80.40	19.88
$\bar{I} \pm \sigma$ , (J)	299.72 $\pm 0.37$	298.28 $\pm 1.64$	284.65 $\pm 10.22$	253.79 $\pm 44.75$	194.12 $\pm 14.67$	126.86 $\pm 12.73$	95.98 $\pm 12.77$	43.29 $\pm 20.81$

Now—a—days, brittle fracture in tension for SDSS aged at 475 °C has not been reported in the literature, at list for the range of times presented in this work. Failure in tension under monotonic loading conditions at low strain rates, results in a fracture of ductile nature, even for aged conditions at 475 °C. Thus, from a fractographic analysis alone, it is not possible to estimate, even in a qualitative fashion, the changes in mechanical properties in tension for SAF 2507 SDSS. Figure 8 represents the lowest, the highest and the intermediate time of aging; nevertheless, in comparing the corresponding fractured surfaces, they are indistinguishable. On the other hand, although Table 1 reports a little difference of 6.5% in ductility between the “0 h aging” and the 288 h aging condition, for the Proof strength,  $R_{p0.2\%}$ , and the Tensile strength,  $R_m$ , the differences were 28% and 25.6% respectively, which indicate a relatively high increase in strength. It is possible that the potential cleavage cracks in ferrite can be

constrained by the elongated austenite lamellae, preventing a final brittle fracture.

### Impact Fracture Behavior

Impact toughness is one of the most important mechanical properties of metallic materials and its alloys. On the other hand, the most significant effect of the 475 °C embrittlement of DSS and SDSS is the sudden drop in impact toughness limiting the upper service temperatures in many applications. Note that besides  $\alpha'$ , other phases that impair the impact toughness are formed in DSS and SDSS [18,75,76], but generally at temperatures higher than  $\approx 550$  °C [77,46,63,78–82]. Contrary to the tensile fractured samples, the evolution of the fractured surfaces of the impact samples with the aging time, showed a transition between ductile and brittle behavior, which in turn, is reflected in the values of impact toughness (Table 2, [18]). Then, the morphologies of the fractured surfaces shown in figures 9—a, 9—b and 9—c (3, 72 and 192 h of

aging respectively), represent the ductile, transitional and brittle behavior of the SAF 2507 SDSS.

A detailed microscopic analysis of the impact fracture surfaces which correspond to the ductile behavior, showed that the topographic features were similar to those showed in figure 8, *i.e.*, the MC was the observed mechanism of fracture. From Table 2 is easy to see that the values of the impact toughness for 3, 9, and 24 h of aging, are statistically equivalent, and similar to that of the as-received + solution treated condition (299.72 J). Then, averaging over the entire range of the respective data (0–24 h of aging), the average absorbed energy corresponding to these “low times of aging” becomes  $\approx$

284 J. This level of absorbed energy obeys to the inherent high toughness of the studied alloy. So, the fracture behavior of the impact samples for the steel aged between 0 and 24 h, can be regarded as ductile. On the other hand, the microscopic analysis of both, transitional and brittle behavior, will be based on figure 9–d, which shows a brittle fracture surface related with the aging time of 288 h. This stands on the fact that the corresponding fractured surfaces reveal very similar fractographic characteristics, in despite that the corresponding impact energy values were very different (*i.e.*, (194.12; 95.98 and 43.29 J for 72, 192 and 288 h of aging at 475 °C respectively).

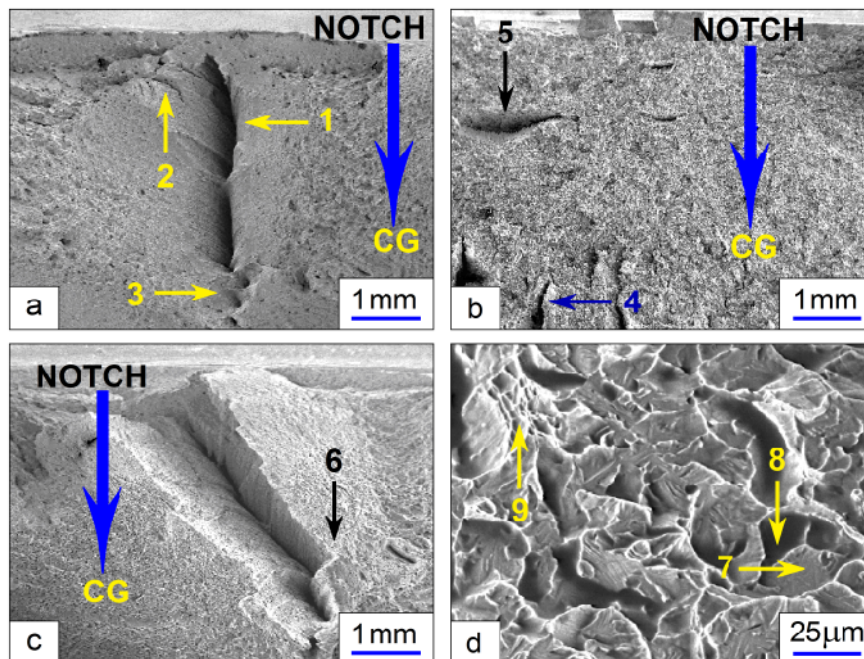


**Fig. 9.** SEM fractographs of the broken impact samples of SAF 2507 SDSS aged for: (a) 3 h, (b) 72 h, (c) 192 h (CG = Crack Growth direction), (d) 288 h.

The macroscopic analysis of figures 9–a, 9–b and 9–c is as follows: The 5 impact samples aged for 3h, showed an average impact toughness of 298.28 J (Table 2, [18]). For this experimental condition, three samples, out of five, presented several “separations” near the notch (Figure 9-a) which are not related with a brittle behavior at all, but is

thought to relax the triaxial stress condition blunting the crack tip, and occur in order to promote the high absorbed energy observed in this samples. This situation is similar to that of the Chao *et al.*, [76], who studying several longitudinal–transverse (LT) V-notched Charpy impact samples of an Fe20Cr5Al alloy aged at 475 °C, observed

this kind of separations. The process which is associated to the formation of the separations was called “ductile delamination”. In figure 9–a (3 h of aging), arrows labeled 1 and 2, show one of these separations and a small secondary crack respectively. This separation develops in a plane parallel to the elongated domains of austenite (in the L direction), and in the direction of growth of the advancing main crack separations and a small secondary crack respectively. This separation develops in a plane parallel to the elongated domains of austenite (in the L direction), and in the direction of growth of the advancing main crack (that crack which forms the fracture surface) as can be observed in figure 10–d (schematic), which shows a separation positioned in a vertical orientation. In figure 9–a, the main crack grows in the CG (crack growth) direction. The arrow labeled 3 in figure 9–a, pointed to a group of voids in the lower part of the separation. Apparently, the plasticity related with these voids, arrested the separation, preventing its further development.

Figure 9–b shows a fractograph which corresponds to 72 h of aging, and represents the first serious drop in impact toughness experienced for the studied alloy. With regard to the average impact toughness value for 72 h of aging (194.12 J), it decreases 32% as compared to the steel aged between 0 and 24 h (see Table 2, [18]). This condition can be considered a transitional one between ductile and brittle behavior. The fracture surface in figure 9–b is characterized by the presence of numerous small cracks, which cannot be regarded as separations, as can be deduced from the sharpness of their tips. These cracks developed in two mutually perpendicular planes, an schematic of which can be observed in figures 10–d and 10–e (considering cracks in place of separations). Arrow 4 in figure 9–b shows a crack similar in orientation to the separation of the figure 9–a, while arrow 5 in figure 9–b, pointed to a crack which has been developed at 90° of the main crack growth direction CG. In despite of its brittle

appearance, the fracture surface shown in figure 9–c (192 h of aging), is associated to an average impact toughness of 95.98 J (Table 2, [18]), that is to say, about one third of the stored impact energy of the as–received material. Although this value of impact toughness is higher than most of the common metallic alloys, the corresponding fracture surface shows a characteristic appearance of a brittle fracture.

In figure 9–c arrow 6 shows a zig–zag type brittle crack, making an angle with the main crack growth direction. The impact fracture surface for the lowest impact toughness (Figure 9–d, 43.29 J), was developed after 288 h of aging. Although this value of impact toughness is higher than the commonly acceptance level of 27 J, the general behavior of the alloy can be regarded as brittle. As has been mentioned earlier, figure 9–d represents the microscopic morphology of the fractured surfaces for the conditions ranged between 72 and 288 h of aging.

The inherent high impact toughness, characteristic of the studied SDSS, can be easily explained in terms of the deformation of the  $\gamma$  islands, as has been proven by Verhaeghe *et. al.*, [69,83]. While low–time aged SDSS fail in a ductile fashion in  $\gamma$  as well as in  $\alpha$  phases, it is certain that for long times of aging, cleavage cracks nucleate in the embrittled ferrite, but their propagation through the microstructure is controlled by the plasticity of the austenite, which remains ductile. Then, the fracture surface is covered by two distinctive features: cleavage facets in the ferrite, and enlarger holes of different morphologies in the austenite. These atypical holes are surrounded by many cleavage facets. Figure 9–d shows a cleavage facet (arrow 7), a typical austenitic hole at 8 and a void sheet or ductile region of fine microvoids at 9. The unique difference between the fracture surface morphology related with the transitional condition (72 h of aging) and the brittle conditions (120, 192 and 288 h of aging), is the number of cleavage facets, which is larger

for the brittle conditions, and the number of austenitic holes, which is larger for the transitional condition. In other words, the transitional condition can be regarded as

one with a smaller degree of brittleness as compared with the brittle conditions.

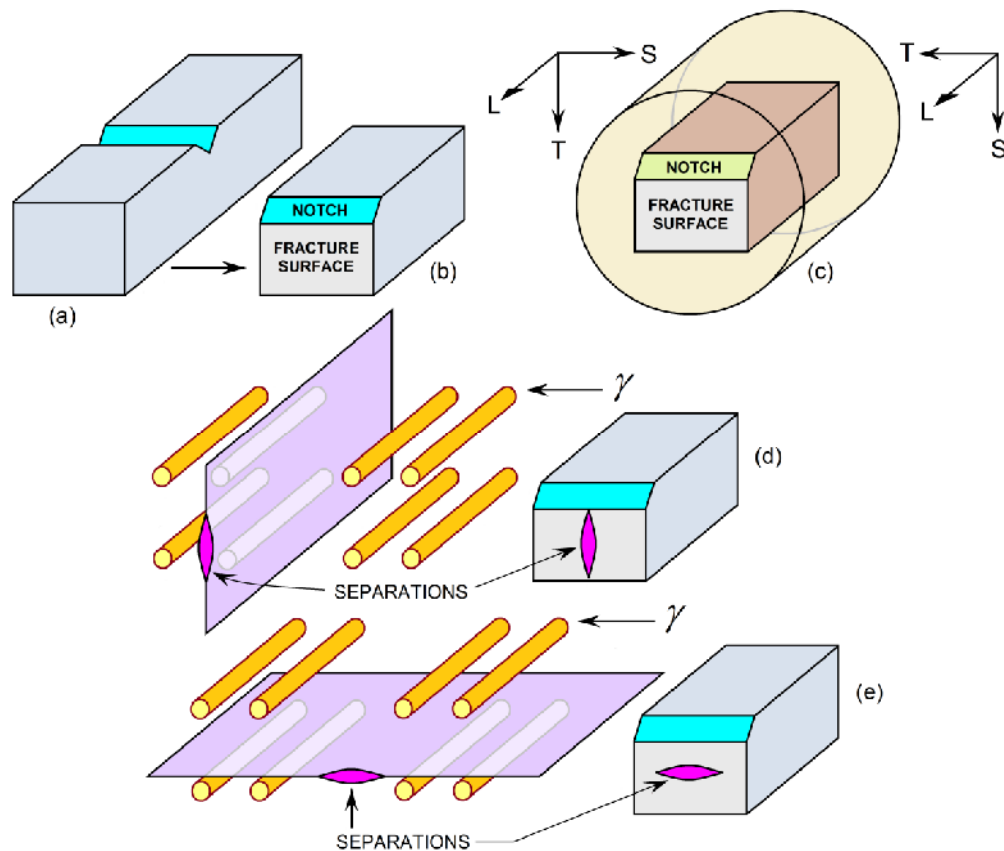


**Fig. 10.** Charpy impact sample (a) before, and (b) after the impact fracture. (c) Fractured impact sample as related with the as-received bar of SAF 2507 SDSS. From the point of view of the cylindrical geometry, the directions T and S are interchangeable and indicate the direction ( $\downarrow$ ) of the advancing main crack which forms the fracture surface. L is the rolling direction. (d) Relation between the plane of a vertical separations (or crack), the  $\gamma$  domains and the impact fracture surface. (e) Relation between the plane of an horizontal separation (or crack), the  $\gamma$  domains and the impact fracture surface.

### Impact Toughness—Fractal Dimension Relationship

Before analyze the fractal characteristics of the impact fracture surfaces of the studied alloy, some observations must be made about the island's morphology. Figure 11 reveals the morphology evolution of some islands developed on specific regions of the impact fracture surfaces, after several grinding and polishing operations. Figures 11—a to 11—g, correspond to an impact sample in the as-received + solution treated condition (ductile behavior) and figures 11—h to 11—m, to a sample aged for 120 h

(brittle behavior). If a comparison should be made between these two groups of islands, it must be about the tortuosity of the contours and size of the islands, as they are the most evident features which constitute its character. At a first glance, it is very difficult to distinguish what island, or group of islands, has a rougher contour. On the other hand, it is possible that for a ductile material, the grinding and polishing operations performed on the fracture surface, erode the net of ridges that made the connection between dimples. This net commonly

expands over large areas of the fractured surface. As a result, the obtained flat islands are larger than the corresponding to a brittle fracture, in which the many cleavage facets are not inter-connected in the same way than the net of ductile ridges, but oriented at different angles, with the particular grain involved. Of course, more important than the contour or the size of islands, is the rate at which the total perimeters of the islands for the metallographic layers, changes with respect to the total

area of the islands covered by these perimeters in the same layers. In this consideration resides the very nature of the definition of fractal dimension based on the SIM. Nevertheless, for the studied SAF 2507 SDSS, and may be for other metallic alloys, it is important to mention the size of the islands as a possible factor to consider in the analysis of the ductile-to-brittle impact fracture transition behavior.

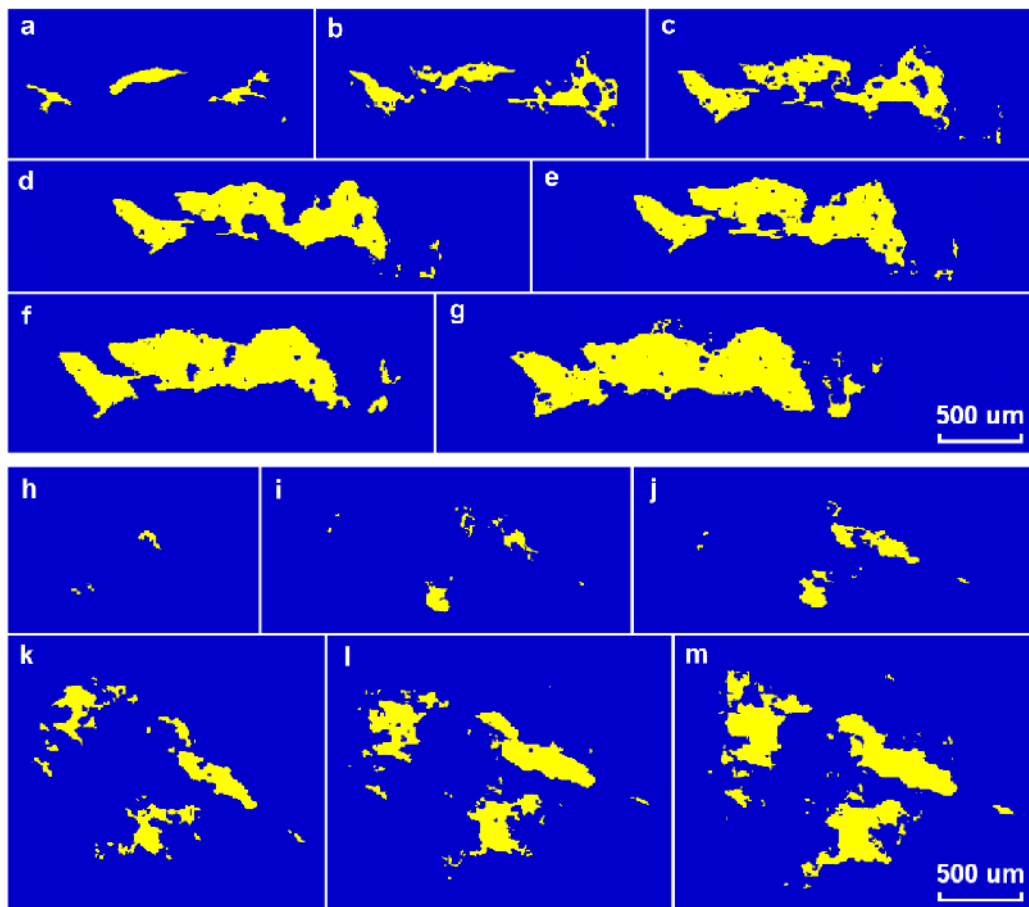


**Fig. 11.** Metallic islands after final digitalization. (a), (b), (c), (d), (e), (f), (g) represent 7 nonconsecutive partial layers (out of 12), developed to calculate the value of  $(D_f)^* = 0.33$ , corresponding to a broken unaged impact sample (as-received + solution treated condition). (h), (i), (j), (k), (l), (m) represent 6 nonconsecutive partial layers (out of 20), developed to calculate the value of  $(D_f)^* = 0.14$ , corresponding to a broken impact sample aged for 120 h at 475 °C.

**Table 3.** Fractal dimensional increments  $(D_T)^*$  and  $(D_I)^*$ 

t (h)	0	3	9	24	72	120	192	288
$(D_T)^*$	0.34	0.32	0.28	0.27	0.23	0.15	0.11	0.09
$(D_I)^*$	0.33	0.34	0.34	0.32	0.21	0.14	0.11	0.09

Table 3 shows the fractal dimensional increment values for tension and impact fracture surfaces,  $(D_T)^*$  and  $(D_I)^*$  respectively. It can be seen that the values of  $(D_I)^*$ , for the times of aging between 0 and 24 h are very close (ranging between 0.32 and 0.34) because of the similar pattern of fracture. For these high toughness ductile fracture surfaces, as the matrix undergoes plastic deformation, the localized stress state and the presence of inclusions, induces void formation at the interfaces inclusion–austenite and inclusion–ferrite. As the voids grow, they form deep holes, and the fracture occurs. The fracture surfaces show sudden general changes in the corresponding topography (ridge–and–valley profiles). These changes are responsible for the high values of  $(D_I)^*$ . A departure from this uniform behavior is showed in Table 3 for the material aged between 72 and 288 h. The continuous increase in precipitation of phase  $\alpha'$  in this range of aging is responsible for the decrease in impact toughness observed in Table 2 [18], as compared to the respective values obtained between 0 and 24 h. In despite of this, these levels of stored energy by impact are still considered very high, which reveals that this high impact toughness behavior is inherent to the SAF 2507 SDSS. The cause for this high toughness behavior lying in the plasticity of the austenite, which prevents the expansion throughout the material of the cleavage cracks nucleated in the embrittled ferrite. These cracks are arrested at the ferrite/austenite interface. On the other hand, as the time of aging increases, the number of cleavage facets increases too. Then, the angle between the cleavage facets and the mean plane of fracture decreases,

generating a lower surface relief which finally leads to a decrease in  $(D_I)^*$ .

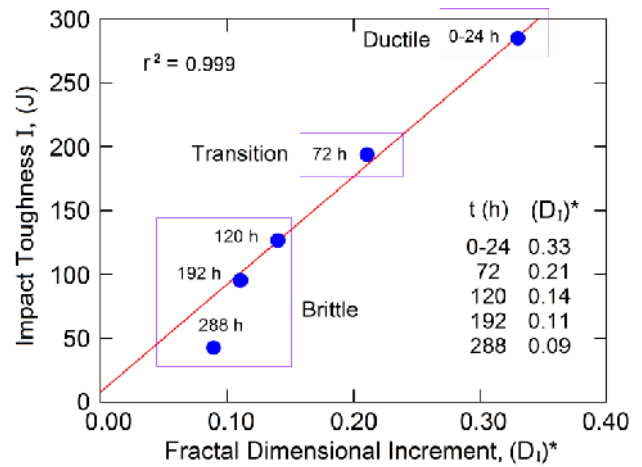


**Fig. 12.** Impact toughness at room temperature as a function of the fractal dimensional increment, for SAF 2507 SDSS aged at 475 °C. [18].

Based on the fractal dimension and impact toughness data collected in this work, the diagram shown in figure 12 was developed. Note that the data corresponding to the treatments performed between 0 and 24 h are statistically uniform, thus, they have been averaged [Impact toughness  $I = 284$  J;  $(D_I)^* = 0.33$ ]. This datum represents the ductile behavior, as indicated. Another important thing to mention concerns with the data of the impact toughness value for 288 h of aging, which show a large dispersion ( $\sigma = \pm 20.81$  J) around the corresponding low average impact toughness of 43.29 J. In consequence the datum  $(D_I)^* = 0.09$ ;  $I = 43.29$  J, was not included in the statistical linear correlation presented in figure 12. Then, for the rest of the data (0-24; 72; 120 and 192 h), the squared correlation coefficient was  $r^2 = 0.999$ . The data for the ductile, transition and brittle behavior have been highlighted in figure 12. Hilders and Zambrano [18], have been shown that the relation between  $I$  and  $(D_I)^*$  represented in figure 12 can be written as:

$$I = I_o + A(D_I)^* = I_o + \frac{\pi}{4} \ell E (\lambda a_o)^2 (D_I)^* \quad (2)$$

where  $I_o = 7.52$  J is the minimum value of  $I$  for  $(D_I)^* = 0$ ;  $A = 849$  J, is a constant composed of  $EV_c$ ,  $E =$  Young's modulus and  $V_c = [\pi (a_c/2)^2 \ell]$  a critical cylindrical volume of material, being  $\ell$  the length of the cylinder and  $a_c$  its diameter (critical length). The parameter  $\lambda = a_c/a_o$ , where  $a_o$  represents a sub-unit of  $a_c$  (material dependent structure parameter), is the number of these sub-units that must join together to conform a critical length. As has been recently quoted by Carney and Mecholsky [55], Ritchie *et al.*, [84], suggested that a critical length (which can be called a "microstructurally significance distance"), of 100–300  $\mu\text{m}$  could be related with the unstable crack propagation in metallic alloys. In the present case,  $a_c = 2(V_c/\ell\pi)^{1/2}$ . As  $A = 849$  J = 849 Nm =  $EV_c$ ; where the value of  $E$  is  $200 \times 10^9$  N/m<sup>2</sup> [85], and  $\ell$  can be taken as 10 mm; then,  $V_c = 4.25 \times 10^{-9}$  m<sup>3</sup> or 4.25 mm<sup>3</sup>, and  $a_c = 0.736 \times 10^{-3}$  m = 736  $\mu\text{m}$ .

It is pertinent to indicate that  $V_c$  is associated to the total length of the crack front, and resembles the classical plastic zone, which spreads along the crack front across the thickness of the samples used in linear elastic fracture mechanics. Thus, as a consequence,  $\ell$  becomes as large as the corresponding crack front (of a standard Charpy sample), *i.e.*,  $\ell = 10$  mm. Finally,  $a_o$  has been taken as the size of a "generic" structural parameter: the largest cleavage facet for brittle fracture, and the largest dimple for ductile fracture, both of them with approximately the same size: 30  $\mu\text{m}$  [18]. From the values of  $a_c$  and  $a_o$ ,  $\lambda = 736 \mu\text{m}/30 \mu\text{m} \approx 24.5$ . The concept of critical volume of material was partially based on the notion of the non-equilibrium fracture process type suggested by Mecholsky *et al.*, [86], which begins with separation of primary bonds at the atomic level, creating a free volume as a result of discrete geometric reconfigurations along the tip of a crack front.

A great deal of research into the fundamental relations connecting fractal characteristics of fractured surfaces and mechanical properties, has been performed by Mecholsky

and co-workers [55,86–90], especially in ceramic materials, though many concepts developed by them are equally applicable to metallic alloys. Although several authors have studied the relationship between impact toughness and  $D$  [49,52,54,91,92], some others have been made emphasis in the connection between the fracture toughness and  $D$  [55,93–95]. Particularly, Carney and Mecholsky [55], analyzed the relation between  $K_{IC}$  and the fractal dimensional increment  $D^*$  for 4340 steel, using the previously developed concept of  $a_o$  (material dependent structure parameter) for ceramics. In despite of how the toughness is measured, it is clear that the introduction of a structure parameter can facilitate the comprehension of the relation between this property and  $D$ . Since  $a_c = \lambda a_o$ , the slope of the linear relation [equation (2)], which has been represented in figure 12 is:

$$A = \frac{dI}{d(D_I)^*} = \left( \frac{\pi \ell E}{4} \right) a_c^2 \quad (3)$$

It is clear from equation (3), that the critical length for unstable crack propagation  $a_c$ , can be estimated from impact toughness and fractal dimensional increment data (*i.e.*, from the value of the slope  $A$ ). Three zones have been well defined in figure 12: brittle, transition and ductile. Then, as the "low impact toughness–low fractal dimensional increment zone" (brittle zone) corresponds to the studied SDSS with the largest amounts of precipitated  $\alpha'$  phase, this material can be associated with a less resistance to degradation by corrosion. On the contrary, in the "high impact toughness–high fractal dimensional increment zone" (ductile zone), the material is associated to a good corrosion behavior.

### Tension Properties—Fractal Dimension Relationship

Apart from the work of Richards and Dempsey [96], and that of Hilders *et al.*, [28], few studies have been devoted to the specific study of the relation between tensile properties of metallic materials and the corresponding fractal characteristics of the fractured surfaces. One reason for

this is that too many authors have emphasized the importance of the toughness–fracture topography relationship, as has been already mentioned. In light of the current understanding of plastic flow of polycrystals as a dissipative and non–equilibrium process driven by external stresses [56], and the scale–invariant behavior [97-99] of dislocations, a suitable explanation of the connection between tension fracture surface tortuosity and the strength and ductility can be advanced. Figure 13 shows the relation obtained between the measured mechanical properties in tension, and the respective fractal dimensional increment,  $(D_T)^*$ . Here, the curves corresponding to the strength ( $R_{p0.2\%}$  and  $R_m$ ), were plotted alongside the elongation curve  $EL(\%)$ .

As expected, the ductility decreases as the time of aging increases, whereas both,  $R_{p0.2\%}$  and  $R_m$  increase. The arrows on the curves in figure 13 point to the increase of aging time. On the other hand, it is observed that the higher the time of aging at 475 °C, the lower the fractal dimension of the fractured surfaces. In other words, as the irregularity of the fractured surfaces decreases, the material becomes less ductile and stronger. The plastic flow phenomenon which occurs in a material undergoing tensile deformation, manifests in the development of cell configuration of groups of dislocations, which exhibit a fractal structure [97,98]. The evolution of the plastic flow denotes a higher complexity and density of these groups of dislocations, increasing its fractal dimension. According to Vinogradov *et al.*, [56], if any metallic polycrystal becomes plastically deformed, a deformation relief is formed on its surface, being the features of the surface relief affected by the bulk microstructure evolving with strain.

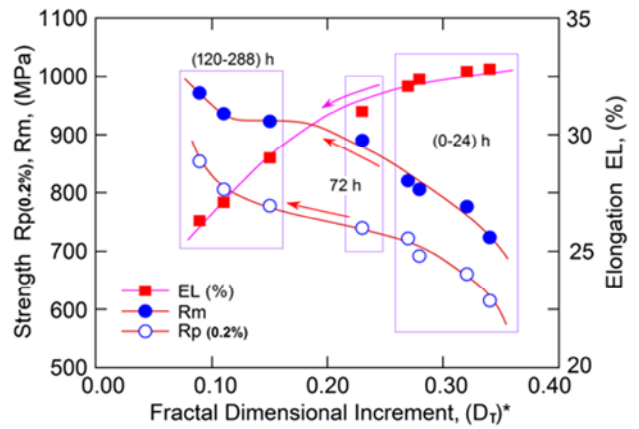


**Fig. 13.** Strength and ductility at room temperature as a function of the fractal dimensional increment, for SAF 2507 SDSS aged at 475 °C.

Zaiser *et al.*, [100], using atomic force microscopy and white light interferometry, studied the surface profile of deformed 99.99% purity polycrystalline copper and analyzed the changes in the respective fractal dimension, suggesting that the quantities measured at the surface can represent the behavior of the bulk. Thus, the fractal dislocation structure can be reflected in the fractal surface relief. In the same way, it is suggested that the changes in the fractality of the bulk microstructure of dislocations, can be translated to the corresponding fractal characteristics of the fractured surfaces. Then, it is easy to deduce that these changes of the microstructure affect the macroscopic mechanical properties, which in turn must be reflected in the fracture surface roughness.

Vinogradov *et al.*, [56] used the stress–strain curve as a rational basis to study the evolution of the microstructure which occurs in a sample undergoing plastic deformation to fracture. They used white light interferometry and acoustic emission during uniaxial tensile deformation, to monitor the fractal dimension of the dislocation structure, which evolves during the process of plastic deformation in several polycrystals of Cu (99.96% and 99.98% purity, with grain size ranged between 36 and 170  $\mu\text{m}$ ) and Al (99.999% purity, with a grain size of 120  $\mu\text{m}$ ). Assuming

that the dislocation cell structures are self-affine configurations [97], Vinogradov *et al.*, [56], used an equation which matches the experimental stress-strain curves obtained for both, the common coarse-grained materials [101], and the ultrafine-grained ones [102]. This equation is written as:

$$\sigma = \frac{\alpha \mu M}{k_2} \left( \alpha k_0 \frac{D_d - 1}{D_d} + k_1 \right) \left[ 1 - \exp\left(-\frac{k_2 M \varepsilon}{2}\right) \right] \quad (4)$$

where  $\sigma$  is the engineering stress;  $\varepsilon$  is the engineering strain;  $\alpha$  is a numerical factor of the order of 0.3–0.5;  $\mu$  is the shear modulus;  $M$  is the Taylor factor, which is determined by the crystallographic texture showed by the polycrystal;  $D_d$  is the fractal dimension of the average dislocation cell, and  $k_i$  ( $i = 0,1,2$ ) are strain-independent phenomenological kinetic coefficients which can be estimated from the stress-strain curves [103]. In the equation (4),  $D_d = D_d(\varepsilon, \sigma)$ , for the complexity of the dislocations groups, increases as the strain and stress increased. It is possible to relate  $D_d$  in an explicit manner, with the strain hardening coefficient  $\theta = d\sigma/d\varepsilon$  [104] as:

$$D_d = \alpha k_0 / \left[ \alpha k_0 + k_1 - \frac{1}{\alpha M \mu} \left( k_2 \sigma + \frac{2}{M} \frac{d\sigma}{d\varepsilon} \right) \right] \quad (5)$$

According to the equation (5) and taking into account that  $\sigma$  and  $d\sigma/d\varepsilon$  simultaneously changes during the progress of tensile deformation, an increase in  $D_d$  must be observed for the condition  $|\Delta\sigma| > |\Delta(d\sigma/d\varepsilon)|$ . After the plastic instability develops in the material [necking or Considère point, in which:  $(d\sigma/d\varepsilon)|_{\varepsilon n} = \sigma(\varepsilon n)$ ], a decrease in  $D_d$  is observed as the condition  $|\Delta\sigma| < |\Delta(d\sigma/d\varepsilon)|$  holds. In other words, the fractal dimension of the microstructure (dislocations cells), evolves during the deformation process. From this point of view, we assume that  $D_d$  does represent microstructural evolution. As for the studied alloy the plastic deformation between the strain instability and the fracture point is small, as compared with the total

deformation, for practical purposes it can be considered that the net effect of the deformation process is to increase the value of  $D_d$ .

Although the data in figure 13 is related with eight different tests, we can use equation (5) to substantiate the observed trends obtained for the strength and ductility of the aged SDSS broken in tension. In other words, in our experiments the increase in  $Rp_{0.2\%}$  or  $Rm$  is not related to the increase in  $\varepsilon$  for a particular test, but to a general decrease in ductility, because the raise in the aging time. So, in our experiments as  $Rp_{0.2\%}$  and  $Rm$  increase (lower times of aging, representing seven different tests from the “0 h aging condition”), the values of  $El(\%)$  decreases, which is in line with the observed decrease in  $(D_T)^*$ .

As is very well known, the breaking of bonds with original atom neighbors, and then reforming bonds with new neighbors corresponds to a plastic (nonrecoverable) deformation, accomplished by means of the movement of dislocations. This process has been called slip. When the interaction between dislocations and certain obstacles (solute atmospheres, second phase particles, etc.) is significative, it is found that the departure from elastic to plastic behavior in the stress-strain curve (the onset of plastic deformation), shows sharp irregularities. On the contrary, some metallic alloys which experience a gradual elastic-plastic transition, show a smooth stress-strain curve. The latter behavior is the one which corresponds to the studied SDSS. In this case, the interaction between the moving dislocations and the  $\alpha'$  phase is enough to raise the proff strength after a plastic strain of 0.002 without any visible effect on the stress-strain curve. The reason for this is the already mentioned extremely low lattice mismatch between  $\alpha'$  and  $\alpha$  phases, responsible for the low elastic coherent strain energy of the  $\alpha/\alpha'$  interface, which facilitates the movement of dislocations throughout the  $\alpha'$  phase.

The amount of  $\alpha'$  which is larger for higher times of aging, leads to an increased resistance to the dislocation motion into the ferrite, which corresponds to an increase in  $R_{p0.2\%}$ , as depicted in figure 13. With increasing applied stress beyond  $R_{p0.2\%}$ , more dislocations are created, and the stress to continue the strain hardening stage of the alloy, steadily increases to its maximum value  $R_m$ . Then, as  $R_m$  depends significantly on strain hardening, the complexity of the dislocation structures developed at this point is very high. It must be remarked that the  $R_{p0.2\%}$  and  $R_m$  values, correspond to the alloy as a whole, and nearly re- present the ones for the ferrite phase, which hardens more than the austenite phase. Figure 13 shows the similar qualitative behavior of the  $R_{p0.2\%}$  and  $R_m$  values, which increase as the time of aging increases, and the values of  $El(\%)$  and  $(D_f)^*$  decrease.

Although the tension behavior shown in figure 13 cannot be directly related with changes in the fracture surface morphology, as was the case for the impact toughness in figure 12, specification of the fractal dimensional increment values of the fractured surfaces in tension (which were generated for different microstructures within the aged material), can be an alternative way to characterize the ductility and strength properties. The three zones delineated in figure 13 are related with low, transitional and high values of fractal dimensional increment (120 to 288; 72; and 0 to 24 h of aging respectively). In the present work, in addition to the role of the fractal dimensional increment in monitoring the mechanical properties in tension, we note that it has been proven successful to discriminate between fractured surfaces with very similar morphologies. As an example, a close examination of figures 7-a and 7-c, reveals the same macroscopic morphology characteristic of the ductile process developed in the central part of the cup portion of the corresponding fracture surfaces. The respective counterparts of figures 8-a and 8-c, show the microscopic version of the ductile fracture by MC. These fractured surfaces which correspond to the studied alloy

aged for 3 and 192 h respectively, have the very same morphology. Nevertheless, the respective values of  $(D_f)^*$  are very different: 0.32 and 0.11, as can be seen in Table 3.

## CONCLUSIONS

The observations described above for the aged SAF 2507 SDSS can be summarized as follows:

(1) The average impact toughness values for SAF 2507 SDSS, decrease from about 300 to 43 J, as the time of aging at 475 °C increases from 0 to 288 h. In this range of impact toughness's, a complete transition from ductile to brittle behavior occurred, although it is considered that the impact toughness value of 43 J is still high enough, as compared with the lowest accepted level for many commercial alloys (27 J).

(2) For aging times between 0 and 24 h, the impact behavior of the studied material was of the ductile type, being the average value of impact toughness  $\approx 284$  J, and the average fractal dimensional increment  $(D_f)^* \approx 0.33$ .

(3) After 72 h of aging, the impact fracture surfaces of the studied material show a mixture of cleavage facets in the  $\alpha$  phase, and enlarger holes of different morphologies in the austenite. This condition has been regarded as a transitional one, and the associated values of  $I$  and  $(D_f)^*$  were 194 J and 0.21 respectively.

(4) For 120, 192, and 288 h of aging, the corresponding impact fracture surfaces were of the brittle type, being the fracture surface morphologies, similar than the one for the transitional condition, but with a larger number of cleavage facets in the ferrite phase, and a smaller number of holes in the austenite phase. As the time of aging increases from 120 to 288 h, the number of cleavage facets increases and the number of holes decreases. Cleavage cracks nucleate in the embrittled ferrite, but

their propagation through the microstructure is controlled by the plasticity of the austenite, which remains ductile. The highest and lowest values of  $I$  and  $(D_I)^*$  in this range were 127 J–43 J, and 0.14–0.09 respectively.

(5) It is shown that the relation  $I$  vs  $(D_I)^*$  was of a linear positive type for the SAF 2507 SDSS. This relation was described by an impact fracture mechanism based on a critical volume (cilinder) of material, with diameter  $a_c$  (a material microstructurally significant distance) developed ahead of the crack tip, and a material dependent structure parameter  $a_o$ .

(6) Tension samples broken at room temperature reveal that the Proof strength  $R_{p0.2\%}$  increases from 614 to 854 MPa (28% increment); and the Tensile strength  $R_m$  increases from 723 to 972 MPa (25.6% increment), as the time of aging increases from 0 to 288 h at 475 °C. On the other hand, tensile ductility, as measured by  $El(\%)$ , barely decreases in 6.5% (from 32.8% to 26.3%) for increased aging times at 475 °C. All the samples for the complete range of aging times, failed by the microvoid coalescence mechanism (MC).

(7) For the SAF 2507 SDSS aged between 0 and 288 h at 475 °C and broken in tension, specification of  $(D_T)^*$  can be a good alternative way to characterize ductility and strength properties. In addition to this role, the values of  $(D_T)^*$  have been successful to discriminate between fractured surfaces with similar morphologies, as the ones obtained in the present work (failure by MC) for all the studied experimental conditions.

(8) The values of  $(D_T)^*$  related to the tension fracture surfaces of the studied steel, although slightly different to its counterparts obtained by impact, follow a similar trend: as the time of aging increases,  $(D_T)^*$  and  $(D_I)^*$  decrease. The values of the fractal dimensional increment for

tension and impact fracture surfaces are the same, only for the aging times of 192 and 288 h.

## ACKNOWLEDGEMENTS

The authors are grateful for the financial support of the Division of Graduate Studies of the Engineering Faculty at the Universidad Central de Venezuela (UCV), Caracas, Venezuela, and the technical support (Numerical control lathe), from the Universidad Nacional Experimental Politécnica (UNEXPO), Caracas, Venezuela. O.A. Hilders wish to thank the support from the Electrical Measurements Laboratory at the Materials and Nanotechnology Engineering Center of the Instituto Venezolano de Investigaciones Científicas (IVIC).

## REFERENCES

- [1] Liu X., Zhang C., Li J., Chen W., Zheng Y., Li H., Han P. (2017) “Effect of solution annealing on microstructure evolution and pitting corrosion resistance of SAF 2906 super duplex stainless steel” *Steel Res. Int.* 87:1700023.
- [2] Cojocaru V. D., Șerban N., Angelescu M. L., Cotruț M.C., Cojocaru E. M., Vintilă A.N. (2017) “Influence of solution treatment temperature on microstructural properties of an industrially forged UNS S32750/1.4 410/F53 super duplex stainless steel (SDSS) alloy” *Metals*, 7(6):7060210.
- [3] Wan J., Ruan H., Shi S. (2017) “Excellent combination of strength and ductility in 15Cr–2Ni duplex stainless steel based on ultra fine-grained austenite phase” *Mater. Sci. Eng. A*, 690:96–103.
- [4] Mishra M.K., Rao A.G., Sarkar R., Kashyap B.P., Prabhu N. (2016) “Effect of preaging deformation on aging characteristics of 2507 super duplex stainless steel” *J. Mater. Eng. Perf.* 25(2):374–381.
- [5] Mohammed G. R., Ishak M., Aqida S. N., Abdulhadi H.A. (2017) “Effects of heat input on

- microstructure, corrosion and mechanical characteristics of welded austenitic and duplex stainless steels: A review” *Metals*, 7(2):7020039.
- [6] Sadeghian M., Shamanian M., Shafyei A. (2014) “Effect of heat input on microstructure and mechanical properties of dissimilar joints between super duplex stainless steel and high strength low alloy steel” *Mater. Design*, 60:678–684.
- [7] Neto J.O., da Silva R. O., da Silva E.H., Moreto J.A., Bandeira R.M., Manfrinato M.D., Rossino L.S. (2016) “Wear and corrosion study of plasma nitriding F53 super duplex stainless steel” *Mater. Res.* 19(6):1241–1252.
- [8] Tucker J.D., Miller M.K., Young G.A. (2015) “Assessment of thermal embrittlement in duplex stainless steel 2003 and 2205 for nuclear power applications” *Acta Mater.* 87:15–24.
- [9] Park H.J., Lee H.W. (2014) “Effect of alloyed Mo and W on the corrosion characteristics of super duplex stainless steel weld” *Int. J. Electrochem. Sci.* 9:6687 - 6698.
- [10] Zhang B., Xue F., Li S. L., Wang X.T., Liang N.N., Zhao Y. H., Sha G. (2017) “Effect of thermal aging on microstructural evolution of ferrite in duplex stainless steel in nuclear power plant applications” *Mater. Sci. Forum*, 898:818–825.
- [11] Magnani M., Terada M., Lino A.O., Tallo V.P., da Fonseca E. B., Santos T. F. A., Ramirez A. J. (2014) “Microstructural and electrochemical characterization of friction stir welded duplex stainless steels” *Int. J. Electrochem. Sc.* 9:2966–2977.
- [12] Zhang Z., Zhao H., Zhang H., Hu J., Jin J. (2017) “Microstructure evolution and pitting corrosion behavior of UNS32750 super duplex stainless steel welds after short-time heat treatment” *Corros. Sci.* 121:22–31.
- [13] Jinlong Lv., Tongxiang L., Limin D., Chen W. (2016) “Influence of sensitization on microstructure and passive property of AISI 2205 duplex stainless steel” *Corros. Sci.* 104:144–151.
- [14] Eghlimi A., Shamanian M., Eskandarian M., Zabolian A., Szpunar J. A. (2015) “Characterization of microstructure and texture across dissimilar super duplex/austenitic stainless steel weldment joint by super duplex filler metal” *Mater. Charact.* 106:27–35.
- [15] Lasebikan B.A., Akisanya A.R. (2014) “Burst pressure of super duplex stainless steel pipes subject to combined axial tension, internal pressure and elevated temperature” *Int. J. Pres. Ves. Pip.* 119:62–68.
- [16] Lee C.H., Chang K.H. (2013) “Failure pressure of a pressurized girth-welded super duplex stainless steel pipe in reverse osmosis desalination plants” *Energy*, 61:565–574.
- [17] Olabarria P.M.G. (2015), *Constructive Engineering of Large Reverse Osmosis Desalination Plants*. Chemical Publishing, Los Angeles, USA.
- [18] Hilders O.A., Zambrano N. (2014) “The effect of aging on impact toughness and fracture surface fractal dimension in SAF 2507 super duplex stainless steel” *J. Microsc. Ultrastruct.* 2(4):236–244.
- [19] Shamanth V., Ravishankar K.S. (2015) “Dissolution of alpha-prime precipitates in thermally embrittled S 2205–duplex steels during reversion-heat treatment” *Results Phys.* 5:297–303.
- [20] Solomon H. D., Levinson L.M. (1978) “Mössbauer effect study of 475 °C embrittlement of duplex and ferritic stainless steels” *Acta Metall.* 26(3):429–442.
- [21] Sahu J.K., Krupp U., Ghosh R.N., Christ H.J. (2009) “Effect of 475 °C embrittlement on the mechanical properties of duplex stainless steel” *Mater. Sci. Eng. A*, 508(1–2):1–14.
- [22] Hedström P., Huyan F., Zhou J., Wessman S., Thuvander M., Odqvist J. (2013) “The 475 °C embrittlement in Fe–20Cr and Fe–20Cr–X (X =

- Ni,Cu,-Mn) alloys studied by mechanical testing and atom probe tomography” *Mater. Sci. Eng. A*, 574:123–129.
- [23] Örnek C., Burke M.G., Hashimoto T., Engelberg D.L. (2017) “748 K (475 °C) Embrittlement of duplex stainless steel: Effect on microstructure and fracture behavior” *Metallurgical and Materials Transactions A*, 48(4):1653–1665.
- [24] Armas A.F., Hereñú S., Alvarez–Armas I., Degallaix S., Condó A., Lovey F. (2008) “The influence of temperature on the cyclic behavior of aged and unaged super duplex stainless steels” *Mater. Sci. Eng. A*, 491:434–439.
- [25] Vogt J.B., Massol K., Foct J. (2002) “Role of the microstructure on fatigue properties of 475 °C aged duplex stainless steels” *Int. J. Fatigue*, 24(6):627–633.
- [26] Kolmorgen R., Biermann H. (2014) “Thermo mechanical fatigue behavior of a duplex stainless steel in the range of 350–600 °C” *Int. J. Fatigue*, 65:2–8.
- [27] Di Cocco V., Iacoviello F., Ischia G. (2017) “Duplex stainless steels “475 °C embrittlement”: Influence of the chemical composition on the fatigue crack propagation” *Proc. Struct. Integ.*, 3:299–307.
- [28] Hilders O.A., Ramos M., Peña N.D., Saenz L. (1999) “Effect of 475 °C embrittlement on fractal behavior and tensile properties of a duplex stainless steel” *J. Mater. Eng. Perf.* 8(1):87–90.
- [29] Johansson J., Odén M. (2000) “Load sharing between austenite and ferrite in a duplex stainless steel during cyclic loading” *Metall. Mater. Trans. A*, 31(6):1557–1570.
- [30] Shamanth V., Arun T. N., Ravishankar K. S. (2015) “Effect of alpha prime (A’) precipitate on the mechanical properties of thermally embrittled S2205 duplex stainless steels” *Int. Adv. Res. J. Sci. Eng. Technol.* 2(5):75–78.
- [31] Alhegagi F.A. (2015) “475°C Embrittlement in stainless steels” *Int. J. Sci. Eng. Res.* 6(9):145–154.
- [32] Wu H.C., Yang B., Wang S.L., Zhang M.X., Shi Y. Z. Chen Y.F., Sun Y.H. (2016) “Effect of thermal aging on corrosion fatigue of Z3CN20.09M duplex stainless steel in high temperature water” *Mater. Sci. Eng. A*, 655:183–192.
- [33] Ramkumar K. D., Thiruvengatam G., Sudharsan S. P., Mishra D., Arivazhagan N., Sridhar R. (2014) “Characterization of weld strength and impact toughness in the multi-pass welding of super duplex stainless steel UNS 32750” *Mater. Design*, 60:125–135.
- [34] Topolska S., Łabanowski J. (2015) “Impact-toughness investigation of duplex stainless steels” *Mater. Technol.* 49(4):481–486.
- [35] Silva R., Della Rovere C.A., Kuri S.E. (2016) “Effect of thermal aging at low temperature on the mechanical properties and corrosion resistance of LDX 2404 duplex stainless steel” *Mater. Sci. Forum*, 869:705–710.
- [36] Iacoviello F., Casari F., Gialanella S. (2005) “Effect of 475 °C embrittlement on duplex stainless steels localized corrosion resistance” *Corros. Sci.* 47:909–922.
- [37] Grobner P.J. (1973) “The 885 °F (475 °C) embrittlement of ferritic stainless steels” *Metall. Trans. A*, 4(1):251–260.
- [38] Chandra D., Schwartz L.H. (1971) “Mössbauer effect study of the 475 °C decomposition of Fe–Cr” *Metall. Trans. A*, 2(2):511–519.
- [39] Danoix F., Auger P., Blavette D. (2004) “Hardening of aged duplex stainless steels by spinodal decomposition” *Microsc. Microanal.* 10(3):349–354.
- [40] Armas I.A. (2008) “Duplex stainless steels: Brief history and some recent alloys” *Rec. Pat. Mech. Eng.* 1(1):51–57.

- [41] Ramkumar K.D., Mishra D., Raj B.G., Vignesh M.K., Thiruvengatam G., Sudharshan S.P., Arivazhagan N., Sivashanmugam N., Rabel A.M. (2015) "Effect of optimal weld parameters in the microstructure and mechanical properties of autogenous gas tungsten arc weldments of super duplex stainless steel UNS S32750" *Mater. Design*, 66 (Part A):356–365.
- [42] Sarwar M., Ahmad E., Manzoor T. (2010) "Crack bridging in stress corrosion cracking of duplex stainless steels" *Key Eng. Mater.* 442:445–452.
- [43] Chattoraj I. (2013) "Stress corrosion cracking of duplex stainless steels" *Adv. Mater. Res.* 794:552–563.
- [44] Schulz Z., Wachowiak D. (2014), *Availability and Economics of Using Duplex Stainless Steels*. Corrosion 2014, NACE International, San Antonio, USA, pp. 1–10.
- [45] Guo Y., Hu J., Li J., Jiang L., Liu T., Wu Y. (2014) "Effect of annealing temperature on the mechanical and corrosion behavior of a newly developed novel lean duplex stainless steel" *Materials*, 7:6604–6619.
- [46] Nilsson J.O. (1992) "Super duplex stainless steels" *Mater. Sci. Technol.* 8(8):685–700.
- [47] ASTM E23–07; (2009) "*Standard Test Methods for Notched Bar Impact Testing of Metallic Materials*" Annual Book of ASTM Standards, Philadelphia, USA, American Society for Testing and Materials, Vol. 03.01.
- [48] ASTM E8/E8M–09; (2009) "*Standard Test Methods for Tension Testing of Metallic Materials*" Annual Book of ASTM Standards, American Society for Testing and Materials, Vol. 03.01, Philadelphia, USA.
- [49] Mandelbrot B.B., Passoja D.E., Paullay A.J. (1984) "Fractal character of fracture surfaces of metals" *Nature*, 308(5961):721–722.
- [50] Dauskardt R.H., Haubensak F., Ritchie R.O. (1990) "On the interpretation of the fractal character of fracture surfaces" *Acta Metall. Mater.* 38(2):143–159.
- [51] Milman Y. V., Stelmashenko N. A., Blumenfeld R. (1994) "Fracture surfaces: A critical review of fractal studies and a novel morphological analysis of scanning tunneling microscopy measurements" *Prog. Mater. Sci.* 38:425–474.
- [52] Hilders O.A., Ramos M., Peña N.D., Sáenz L. (2006) "Fractal geometry of fracture surfaces of a duplex stainless steel" *J. Mater. Sci.* 41(17):5739–5742.
- [53] Ostoja–Starzewski M., Li J. (2009) "Fractal materials, beams, and fracture mechanics" *Z. Angew. Math. Phys.* 60(6):1194–1205.
- [54] Tang W., Wang Y. (2012) "Fractal characterization of impact fracture surface of steel" *Appl. Surf. Sci.* 258(10):4777–4781.
- [55] Carney L. R., Mecholsky J. J. (2013) "Relationship between fracture toughness and fracture surface fractal dimension in AISI 4340 steel" *Mater. Sci. Applic.* 4(4):258–267.
- [56] Vinogradov A., Yasnikov I.S., Estrin Y. (2014) "Stochastic dislocation kinetics and fractal structures in deforming metals probed by acoustic emission and surface topography measurements" *J. Appl. Phys.* 115(23):233506-1–233506-10.
- [57] Hilders O. A., Zambrano N., Caballero R. (2015) "Microstructure, strength and fracture topography relations in AISI 316L stainless steel, as seen through a fractal approach and the Hall–Petch law" *Int. J. Met.* 2015(ID624653):10.
- [58] Krivonosova E.A., Krivonosova E.K., Trushnikov D. N. (2017) "Fractal geometry in metallurgy of welding and coatings" *Mater. Sci. Forum*, 893:252–256.
- [59] Mazurek P., Mazurek D.O. (2014) "From the slit–island method to the Ising model: Analysis of

- irregular grayscale objects" *Int. J. Math. Comp. Sci.* 24(1): 49–63.
- [60] Wilson A. (1991) "Estimation of impact toughness as a function of aging temperature and time" Sandvik Steel Internal Report No. 6079, Sandviken, Sweden.
- [61] Hättestrand M., Larsson P., Chai G., Nilsson J. O., Odqvist J. (2009) "Study of decomposition of ferrite in a duplex stainless steel cold worked and aged at 450–500 °C" *Mater. Sci. Eng. A*, 499(1–2):489–492.
- [62] Park C. J., Kwon H.S., Lohrengel M. M. (2004) "Micro-electrochemical polarization study on 25% Cr duplex stainless steel" *Mater. Sci. Eng. A*, 372(1–2): 180–185.
- [63] Wei Z., Laizhu J., Jincheng H., Hongmei S. (2009) "Effect of ageing on precipitation and impact energy of 2101 economical duplex stainless steel" *Mater. Charact.* 60(1):50–55.
- [64] Danoix F., Auger P. (2000) "Atom probe studies of the Fe–Cr system and stainless steels aged at intermediate temperature: A review" *Mater. Charact.* 44 (1–2):177–201.
- [65] Iacoviello F., Di Cocco V., Franzese E., Natali S. (2017) "High temperature embrittled duplex stainless steels: Influence of the chemical composition on the fatigue crack propagation" *Proc. Struct. Integ.* 3:308–315.
- [66] Fisher R.M., Dulis E.J., Carrol K.G. (1953) "Identification of the precipitate accompanying 885 °F embrittlement in chromium steels" *Trans. Am. Inst. Metall. Pet. Eng.* 197:690–695.
- [67] Miller M.K., Bentley J. (1990) "APFIM and AEM investigation of CF8 and CF8M primary coolant pipe steels" *Mater. Sci. Technol.* 6(3):285–292.
- [68] Nilsson J. O., Chai G. (1990) "The Physical Metallurgy of Duplex Stainless Steels" Duplex 2007, International Conference & exposition, Grado, Italy, Associazione Italiana di Metallurgia.
- [69] Verhaeghe B., Louchet F., Cottignies B.D., Bréchet Y., Massoud J.P. (1997) "Micromechanisms of deformation of an austenoferritic duplex stainless steel" *Philos. Mag. A*, 76(5):1079–1091.
- [70] Mcirdi L., Inal K., Lebrun J. L. (2000) "Analysis by X-Ray Diffraction of the Mechanical Behaviour of Austenitic and Ferritic Phases of a Duplex Stainless Steel" *Advances in X-Ray Analysis, International Centre for Diffraction Data 2000, Vol. 42, Pennsylvania, USA*, pp. 397–406.
- [71] Zielinsky W., Witnicki W., Barstch M., Messerschmidt U. (2003) "Non-uniform distribution of plastic strain in duplex steel during TEM in situ deformation" *Mater. Chem. Phys.* 81(2–3):476–479.
- [72] Callister D.W., Rethwisch D. G. (2010) "Materials Science and Engineering" John Wiley & Sons Inc. New York, USA.
- [73] Hull D. (1999) "Fractography: Observing, Measuring and Interpreting Fracture Surface Topography" Cambridge University Press, New York, USA.
- [74] Pineau A., Benzerga A.A., Pardoën T. (2016) "Failure of metals I: Brittle and ductile fracture" *Acta Mater.* 107:424–483.
- [75] Yamada T., Okano S., Kuwano H. (2006) "Mechanical properties and microstructural change by thermal aging of SCS14A cast duplex stainless steel" *J. Nucl Mater.* 350(1):47–55.
- [76] Chao J., Capdevila C., Serrano M., Garcia-Junceda A., Jimenez J. A., Miller M.K. (2014) "Effect of  $\alpha$ - $\alpha'$  phase separation on notch impact behavior of oxide dispersion strengthened (ODS) Fe20Cr5Al alloy" *Mater. Design*, 53:1037–1046.
- [77] Chopra O. K., Chung H. M. (1985) "Aging of cast duplex stainless steels in LWR systems" *Nucl. Eng.Des.* 89(2–3):305–318.
- [78] Akisanya A. R., Obi U., Renton N.C. (2012) "Effect of ageing on phase evolution and mechanical properties of a high tungsten super duplex

- stainless steel” *Mater. Sci. Eng. A*, 535:281–289.
- [79] Pohl M., Storz O., Glogowski T. (2007) “Effect of intermetallic precipitations on the properties of duplex stainless steel” *Mater. Charact.* 58(1):65–71.
- [80] Martins M., Casteletti L. C. (2009) “Sigma phase morphologies in cast and aged super duplex stainless steel” *Mater. Charact.* 60(8):792–795.
- [81] Breda M., Calliari I., Ramous E., Pizzo M., Corain L., Straffelini G. (2013) “Ductile-to-brittle transition in a Zeron® 100 SDSS in wrought and aged conditions” *Mater. Sci. Eng. A*, 585:57–65.
- [82] Pettersson N., Pettersson R.F.A., Wessman S. (2015) “Precipitation of chromium nitrides in the super duplex stainless steel 2507” *Metall. Mater. Trans. A*, 46 (3):1062–1072.
- [83] Verhaeghe B., Louchet F., Bréchet Y., Massoud J.P. (1997) “Damage and rupture mechanism in an austenoferritic duplex steel” *Acta Metall. Mater.* 45(5):1811–1819.
- [84] Ritchie R. O., Server W.L., Wullaert R. A. (1979) “Critical fracture stress and fracture strain models for the prediction of lower and upper shelf toughness in nuclear pressure vessel steels” *Metall. Trans. A*, 10(10):1557–1570.
- [85] Ponthot J. P., Guo W.C., Rauchs G., Zhang W. H. (2009) “Influence of friction on imperfect conical indentation for elastoplastic material” *Trib. Mater. Surf. Interf.* 3(4):151–157.
- [86] Mecholsky J.J., West J.K., Passoja D.E. (2002) “Fractal dimension as a characterization of volume created during fracture in brittle materials” *Philos. Mag. A*, 82(17–18):3163–3176.
- [87] Mecholsky J.J. (2006) “Estimating theoretical strength of brittle materials using fractal geometry” *Mater. Lett.* 60(20):2485–2488.
- [88] Mecholsky J.J. (2012) “Failure Analysis of Ceramics Laminates Using Quantitative Fractography and Fractal Geometry” *Fractography of Glasses and Ceramics VI*, The American Ceramic Society, Varner J. R., Wightman M. (Ed.), Hoboken, USA, *Ceram. Trans.* 230:149–160.
- [89] Mecholsky J.J., Freiman S.W. (1991) “Relationship between fractal geometry and fractography” *J. Am. Ceram. Soc.* 74(12):3136–3138.
- [90] Mecholsky J. J., Passoja D. E., Feinberg-Ringel K.S. (1989) “Quantitative analysis of brittle fracture surfaces using fractal geometry” *J. Am. Ceram. Soc.* 72 (1):60–65.
- [91] Hsiung J. C., Chow Y.T. (1988) “Fractal characterization of the fracture surface of a high strength low-alloy steel” *J. Mater. Sci.* 33(11):2949–2953.
- [92] Hilders O. A., Pilo D. (1997) “On the development of a relation between fractal dimension and impact toughness” *Mater. Charact.* 38(3):121–127.
- [93] Mu Z. Q., Lung C.W. (1988) “Studies on the fractal dimension and fracture toughness of steel” *J. Phys. D: Appl. Phys.* 21(5):848–850.
- [94] Su Y., Lei W.S. (2000) “Relationship between fracture toughness and fractal dimension of fracture surface of steel” *Int. J. Fracture*, 106(3):41–46.
- [95] Li Y., Yue Y.L., Zhang H.T., Wen M. (2013) “Fractal research approach on the fracture SEM image of Ti<sub>2</sub>AlC/TiAl Compound materials” *Rev. Adv. Mater. Sci.* 33:148–153.
- [96] Richards L.E., Dempsey B.D. (1988) “Fractal characterization of fractured surfaces in Ti–4.5Al–5.0Mo–1.5Cr (CORONA 5)” *Scripta Metall.* 22(5):687–689.
- [97] Zaiser M., Bay K., Hähner P. (1999) “Fractal analysis of deformation-induced dislocation patterns” *Acta Mater.* 47(8):2463–2476.
- [98] Zaiser M. (2006) “Scale invariance in plastic flow of crystalline solids” *Adv. Phys.* 55(1–2):185–245.

- [99] Dimiduk D.M., Woodward C., LeSar R., Uchic M. D. (2006) "Scale-free intermittent flow in crystal plasticity" *Science*, 312(5777):1188–1190.
- [100] Zaiser M., Grasset F.M., Koutsos V., Aifantis E.C. (2004) "Self-affine surface morphology of plastically deformed metals" *Phys. Rev. Lett.* 93(19):195507-1–195507-4.
- [101] Estrin Y., Mecking H. (1984) "A unified phenomenological description of work hardening and creep based on one-parameter models" *Acta Metall.* 32 (1):57–70.
- [102] Estrin Y., Vinogradov A. (2013) "Extreme grain refinement by severe plastic deformation: A wealth of challenging science" *Acta Mater.* 61(3):782–817.
- [103] Mecking H., Kocks U.F. (1981) "Kinetics of flow and strain-hardening" *Acta Metall.* 29(11):1865–1875.
- [104] Vinogradov A., Yasnikov I. S., Estrin Y. (2012) "Evolution of fractal structures in dislocations ensembles during plastic deformation" *Phys. Rev. Lett.* 108(20):205504-1–205504-5.